PERGAMON

International Journal of Heat and Mass Transfer 45 (2002) 3517–3527

International Journal of HEAT and MASS TRANSFER

www.elsevier.com/locate/ijhmt

DPIV/T-driven convective heat transfer simulation

X. Ma [a], G.E. Karniadakis [a,*], H. Park [b], M. Gharib [b]

[a] *Division of Applied Mathematics, Center for Fluid Mechanics, Brown University, 182 George Street, Box F, Providence, RI 02912, USA*
[b] *Graduate Aeronautical Laboratories, California Institute of Technology, Pasadena, CA 91125, USA*

Received 18 July 2001; received in revised form 7 February 2002

Abstract

We present a new approach to simulating unsteady heat transfer, with only very few degrees of freedom, by employing directly eigenmodes extracted from DPIV/DPIT experimental data. In particular, we formulate Galerkin low-dimensional systems of the coupled Navier–Stokes and energy equations using hierarchical empirical eigenfunctions extracted from an ensemble of velocity and temperature snapshots. We demonstrate that even severely truncated Galerkin representations (two velocity modes and four temperature modes) produce simulations capable of capturing the dynamics of the flow and heat transfer. This finding is documented by applying proper orthogonal decomposition to water flow past a heated circular cylinder at Reynolds number 610. © 2002 Elsevier Science Ltd. All rights reserved.

1. Introduction

The recent rapid developments in quantitative imaging in flow and heat transfer problems offer the possibility of integrating seamlessly numerical simulation and experiment. In the new computational paradigm, simulation and experiment could become a symbiotic feedback system for effective heat transfer control applications. The degree of integration and form of feedback will depend critically on the efficiency of the simulation. To this end, efficient low-dimensional systems that represent accurately the short-term dynamics of the coupled flow-heat transfer system need to be employed for real time control. In this paper, we address this subject and develop an approach that will make use of instantaneous and simultaneous measurements of the velocity and temperature fields.

The feasibility for flow model reduction can be proved rigorously only for a few simple flows [1], but experimental and numerical evidence suggests that many complex flows exhibit low-dimensionality and can potentially be described by approximate inertial manifolds, e.g. [2]. In [3] a reduced dynamical system for thermal convection was developed and employed to predict accurately the transition process as a function of the Rayleigh number. Also, in [4] a low-dimensional system was found to be very effective for the inverse natural convection problem, which requires repeated numerical solutions of Boussinesq's equation. From these and related studies, it is clear that the key element of a low-dimensional system is its representation through hierarchical and most energetic scales.

The specific problem we consider in this paper is flow and heat transfer past a heated circular cylinder. Earlier numerical work on flows past isothermal cylinders has shown that the wake dynamics in flow past a cylinder exhibits low-dimensionality for both laminar and turbulent states [2,5,6]. This is also true for convective heat transfer as demonstrated in Fig. 1, which is obtained based on results from high resolution direct numerical simulations (DNSs) [7]. The Peclet number is $Pe = 2730$ and the Reynolds number is $Re = 3900$ corresponding to a turbulent wake. In the figure, we plot the eigenvalues of the most energetic modes obtained from an *ensemble* of snapshots of the system at the aforementioned parameter values. The eigenvalues are normalized so that they represent percentage of total energy of the system. We see that only a few modes contribute significantly to the energy while the rest of the modes decay quickly. This indicates that the turbulent wake, at least in this regime, can be represented by only a few degrees of

* Corresponding author. Tel.: +1-401-863-1217; fax: +1-401-863-3369.
E-mail address: gk@cfm.brown.edu (G.E. Karniadakis).

0017-9310/02/$ - see front matter © 2002 Elsevier Science Ltd. All rights reserved.
PII: S0017-9310(02)00071-6

Nomenclature

a_j	velocity modal coefficients	T_∞	free-stream temperature
Re	Reynolds number	M	number of temperature snapshots
β_j	temperature modal coefficients	$\mathbf{U}$	time-average velocity
T	temperature field	Pe	Peclet number
d	cylinder diameter	$\mathbf{V}$	velocity vector field
T_0	time-average temperature	Pr	Prandtl number
N	number of velocity snapshots	V_∞	free-stream velocity

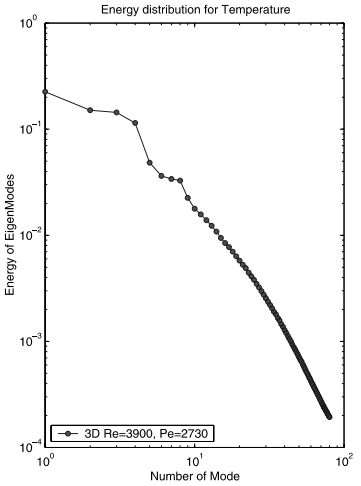

Fig. 1. Eigenspectrum of most energetic temperature modes of turbulent wake. DNS at $Re = 3900$ and $Pe = 2730$.

freedom. Therefore, it can be described by a relatively small set of appropriate basis functions.

The particular approach followed in [5] was based on empirical eigenfunctions derived by proper orthogonal decomposition (POD), while the work in [8] was based on eigenfunctions of a generalized Stokes operator. A comprehensive comparison of these approaches is presented in [9].

Here we will employ POD and work directly with experimental data. POD is a methodology that first identifies the most energetic modes in an evolving system, and second provides a means of obtaining a low dimensional description of the system's dynamics. Background material for the POD approach can be found in the review article in [10]. We adopt the implementation based on the *method of snapshots* developed by Sirovich and co-workers [11]. It has been used so far in conjunction with experimental (e.g. [12–14]) as well as with numerical studies (e.g. [3,5,11,15,16]). However, in previous experiments only point measurements were employed but not images (i.e. snapshots) of vector fields. In the experiments reported here, simultaneous velocity and temperature snapshots were obtained by digital particle image velocimetry (DPIV) and digital particle image thermometry (DPIT), respectively [17–19].

The paper is organized as follows: We first describe the DPIV/T raw data and associated processing required to recover the missing data and to produce a divergence-free basis. We then extract POD modes from the experimental data and from companion DNSs, and compare their corresponding structure. Subsequently, we perform POD simulations based on Galerkin projections and the experimentally obtained eigenfunctions, and we present results that document the effectiveness of this approach. We conclude with a summary and a discussion of employing alternative projections, such as the non-linear Galerkin method.

2. Extraction of POD modes

We have obtained POD modes for the velocity and temperature fields from data sets corresponding to both DPIV and DPIT experiments. In addition, we have performed two-dimensional DNSs and extracted corresponding modes. The simulations were based on spectral/hp element discretization at Reynolds number $Re = 610$ using the code described in [2]; see also [20].

The experiments were performed in a water tunnel facility at Graduate Aeronautical Laboratories at the California Institute of Technology. The water tunnel test section has a cross-sectional area of 15 cm × 15 cm. The freestream velocity can be varied from 3 to 50 cm/s. The freestream temperature can be raised by a bank of staggered heating rods located in the inlet pipe to the diffuser section and can be lowered by a re-circulating chiller (Neslab RTE-110) at the downstream section of the test section. Using a closed-loop temperature controller (Tronac PTC-41), the mean freestream temperature can be maintained within ±0.02 °C at 5 cm/s or within ±0.01 °C at 40 cm/s.

To measure the velocity and temperature of the flow field, the technique of digital particle image velocimetry/thermometry (DPIV/T) is employed. The technique, which was originally developed by Dabiri and Gharib [18] and further improved by Park et al. [19], works by seeding the flow with thermochromic liquid crystal

(TLC) particles. The TLC particles change their reflect wavelength (i.e., color) as function of temperature. By illuminating a two-dimensional cross-section, the velocity and temperature of the flow can be deduced by measuring the displacement and color of the TLC particles, respectively. Because a full spectrum (i.e., white) light source is required to illuminate the TLC particles, a xenon flashlamp assembly was used to illuminate the flow [21]. The flashlamp assembly can be used in similar manner as a pulsed laser to create a short-duration pulse light sheet. The image is captured on a Sony full-frame transfer 3-CCD (R G B; Red, Green, Blue) color camera and then stored on a real-time digital video recorder. For processing, the images in R G B color space are transformed into images of H S I (Hue, Saturation, Intensity) color space. The intensity channel of the image is used to run standard DPIV to compute the velocity field [17]. To compute the temperature, the hue (i.e. color) channel of the image is used. For each TLC particle, a temperature is assigned by comparing its hue value to a priori measured calibration curve of hue versus temperature. The relative temperature uncertainty of individual TLC particles can be large (roughly 10%), but the relative uncertainty at a given location in the image can be reduced to an acceptable level (roughly 2%) by averaging the temperature of particles within a sampling window.

The specific measurements we use here were conducted for a heated circular cylinder of diameter $d = 9.53$ mm in crossflow with freestream velocity 6.4 cm/s and temperature 25.8 °C ; the cylinder surface temperature was maintained at 36.8 °C. The corresponding Reynolds number based on the the cylinder diameter and the freestream velocity is $Re = 610$; the Prandtl number is $Pr = 7.1$. The shedding frequency is $f = 1.405$ Hz and a total of 40 snapshots with time separation between snapshots of 0.066 s were employed in the analysis. The camera, which is placed approximately 2 m from the test section, images an area of 60 mm wide by 50 mm high at the mid-span of the test section.

Typical contour plots of instantaneous streamwise and crossflow velocities are shown in Fig. 2; temperature contours are shown in Fig. 3. The missing velocity data at the upper left corner is due to the shadow of the cylinder where the illumination is too weak for the DPIV to pick up the velocity values. The uncertainty in the mean velocity using a 32×32 pixel sampling window is about 1% and in the temperature is 2%. The disturbance to the flow by the supports is minimized by placing them outside of the two flat end-plates, which have rounded leading edges. The distance between the end-plates is 12.1 cm, and thus the cylinder aspect ratio is $L/d = 13$.

Snapshots of the velocity field obtained from DPIV measurements had missing data because of the shadow region as shown in Fig. 2. Specifically, data was missing

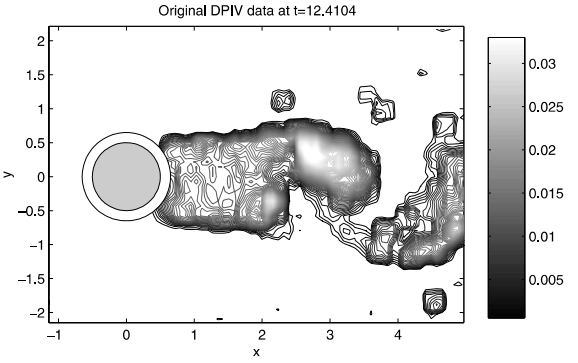

Fig. 3. Contour plots of instantaneous temperature from original experimental (DPIT) data; time $t = 12.4104$ (in non-dimensional convective time units).

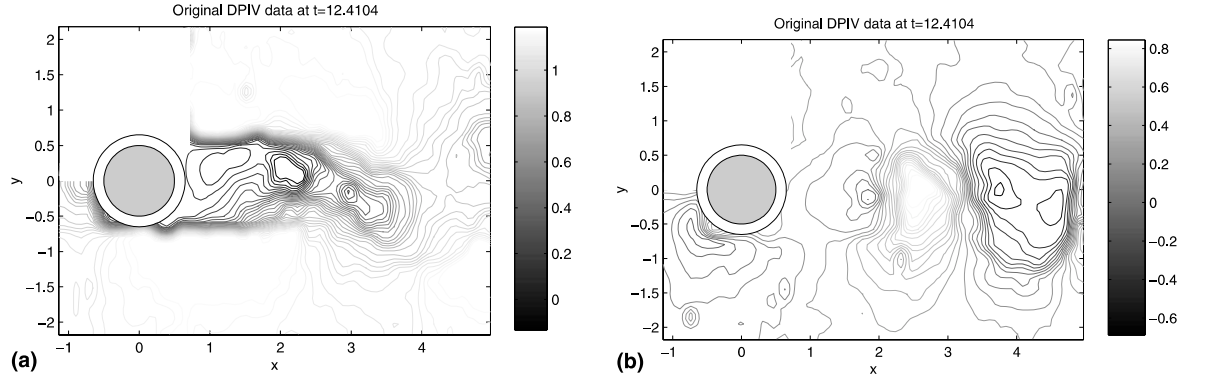

Fig. 2. Contour plots of instantaneous streamwise (a) and crossflow (b) velocity from original experimental (DPIV) data; time $t = 12.4104$ (in non-dimensional convective time units). The domain is shown is the DPIV window with dimensions normalized with the cylinder diameter. DPIV measurements in the area directly above the cylinder were unobtainable because of the shadow cast by the cylinder which was lit from underneath.

in the upper left corner as well as around the cylinder. To handle the first problem, we employed the symmetry properties of POD modes to restore the missing data. To deal with the second problem we interpolated the data between the cylinder surface and the first available points away from the wall, shown as a circle around the cylinder. In addition, we projected the velocity data into a divergence-free field using the Helmholtz decomposition approach; see [7].

Unlike the velocity data, the temperature data is available in the upper left corner of the visualization window. The covariance matrix for the temperature field, constructed from $M = 40$ snapshots, is computed from

$$C_{i,j} = \sum_{m=1}^{N_x} \sum_{n=1}^{N_y} T(x_m, y_n, t_i)\, T(x_m, y_n, t_j),$$

where N_x and N_y are the number of grid points in the x- and y-direction, respectively.

Fig. 4 shows the eigenvalues of the temperature POD modes extracted from experimental data and corresponding two-dimensional DNS data. The velocity POD eigenmode analysis shows a similar distribution, with the important difference that for the velocity field a steep decay occurs after the first two modes.

A comparison between the temperature POD modes obtained experimentally (DPIT) and those obtained from DNS is shown in Fig. 5. The agreement is only qualitative and can be better observed in the higher modes. The main reason for the quantitative disagreement is three-dimensionality induced by the proximity of the side walls in the experiment, in addition to intrinsic flow three-dimensionality at this Reynolds number. From similar comparisons of corresponding velocity POD modes we have observed that there exists a displacement of the DPIV-based modes downstream [7]. This is due to the longer formation length associated with the relatively small aspect ratio ($L/d = 13$) employed in the experiments; see [22,23]. In addition, there is substantial noise in the experimental data above the tenth mode unlike the DNS data, and this explains the slower decay of the spectrum in the high modes.

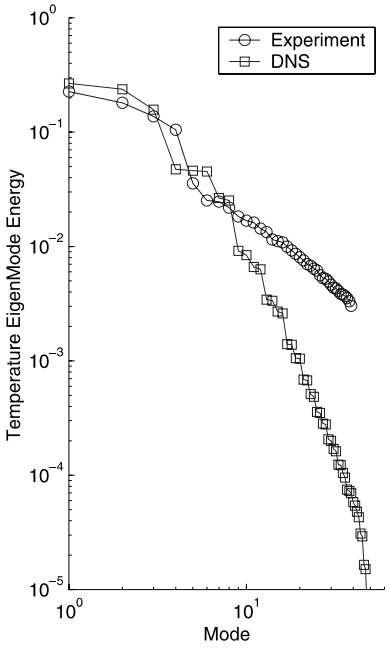

Fig. 4. Comparison of temperature POD eigenvalues between experimental data and DNS data.

These results suggest that in order to represent and simulate accurately and efficiently the convective heat transfer for this problem, we have to employ the DPIT obtained modes as a basis in order to account directly for all the experimental influences. We examine this possibility in the following section.

3. Experiment-based POD simulation

3.1. Formulation

We employ a Galerkin projection of the incompressible Navier–Stokes and energy equations onto these modes in order to construct low-dimensional systems. Let us decompose the velocity vector field $\mathbf{V}$ as

$$\mathbf{V}(\mathbf{x}, t) = \mathbf{U}(\mathbf{x}) + \mathbf{u}(\mathbf{x}, t),$$

where $\mathbf{U}$ is the *time-averaged* field. We express $\mathbf{u}$ as the linear combination of the POD modes

$$u(x, y, t) = \sum_{j=1}^{N} \phi_u(x, y) a_j(t),$$

$$v(x, y, t) = \sum_{j=1}^{N} \phi_v(x, y) a_j(t),$$

where N is the number of velocity snapshots. The Galerkin projection of the Navier–Stokes equation gives

$$\int \boldsymbol{\phi} \cdot \left(\frac{\partial \mathbf{V}}{\partial t} + (\mathbf{V} \cdot \nabla)\mathbf{V} + \nabla p - \frac{1}{R_e} \nabla^2 \mathbf{V} \right) \mathrm{d}\mathbf{x} = 0, \qquad (1)$$

from which we obtain a system of ordinary differential equations (ODEs), which can be solved using Runge–Kutta integration

$$\frac{\partial a_j(t)}{\partial t} = f(\mathbf{a}). \qquad (2)$$

The detailed velocity formulation is presented in [7]. The temperature equation is formulated similarly with the temperature fluctuations $T(\mathbf{x}, t)$ expressed as a finite expansion of bi-orthonormal functions, i.e.

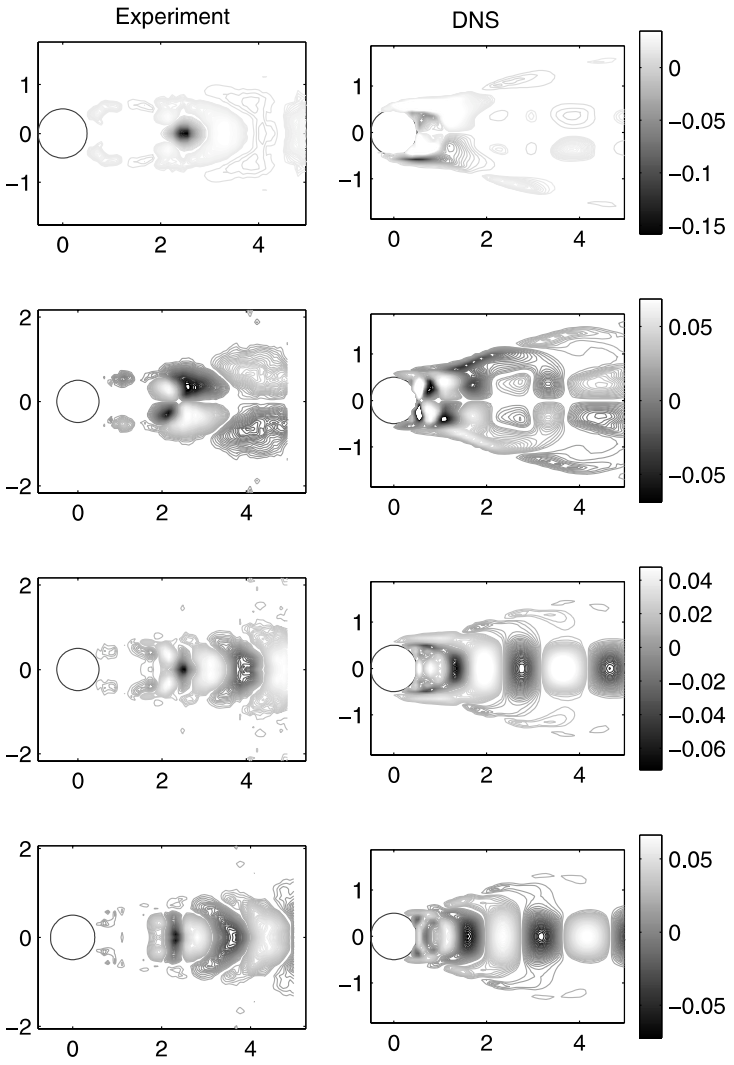

Fig. 5. Comparison between DPIT-based and DNS-based POD modes of the temperature field.

$$T(\mathbf{x},t) = \sum_{m=1}^{M} \beta_m \chi_m(\mathbf{x}) \xi_m(t), \tag{3}$$

where $\chi_m(\mathbf{x})$ are orthonormal POD modes of temperature in the space domain and $\xi_m(t)$ are orthonormal eigenfunctions in the time domain. In Appendix A we give the details of this projection for the interested reader.

3.2. Results

We now compare the POD simulation results with the experimental data. In Fig. 6 we plot the time histories of the velocity modes $a_j(t)$ obtained by the POD simulation and by the projection of the experimental data. We see that good agreement is obtained. In Fig. 7 we compare the POD predictions with corresponding projected experimental data for the streamwise velocity. We see that the differences are very small. We also note the similarity with the instantaneous raw data at the same time instant shown in Fig. 2. More systematic comparisons at different locations downstream of the cylinder of both streamwise and crossflow velocity profiles also show very good agreement [7]. The POD predictions are less accurate closer to the outflow boundary.

A similar comparison is performed in Fig. 8 for the temperature field at time $t = 12.4104$. We see that the differences between the simulation results and the projection results are very small, and that both agree with the instantaneous raw temperature data at the same time instant shown in Fig. 3. A more quantitative comparison between the three sets of data is presented in Fig. 9 that shows instantaneous profiles at downstream locations

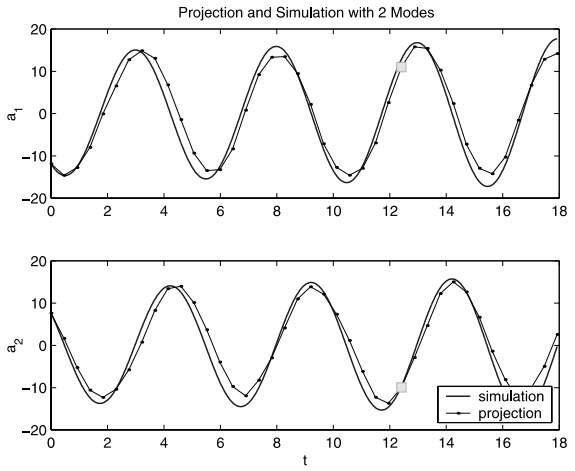

Fig. 6. Comparison of POD simulation and projection using only two DPIV-based POD modes. The time is in non-dimensional convective units.

$x/d = 1.4337$ and $x/d = 2.2377$. There is a noticeable disagreement with the raw data around the centerline of the wake. Finally, a comparison of the histories of the modal coefficients of the temperature over a time of about four shedding periods with the projected experimental data is shown in Fig. 10. We see that overall the POD DPIV/T-based simulation does a very good job in capturing the short-term dynamics of the coupled flow-heat transfer problem even with a very small expansion consisting of two velocity and four temperature modes.

4. Summary and discussion

We have presented a low-dimensional Galerkin approximation of the Navier–Stokes and energy equations in order to simulate convective heat transfer in flow past a heated circular cylinder. The novelty of the method is the direct use of velocity and temperature fields obtained experimentally using DPIV and DPIT. The DPIV/T data form an *ensemble* based on which we extracted the best representation of the velocity and temperature fields (in the average sense) using POD.

An important finding for the cylinder convective heat transfer we study at $Re = 610$ is that only *two velocity* and *four temperature* POD modes are sufficient to describe its short-term dynamics with reasonable accuracy. However, for long-time integration, a Galerkin POD system diverges independently of the number of

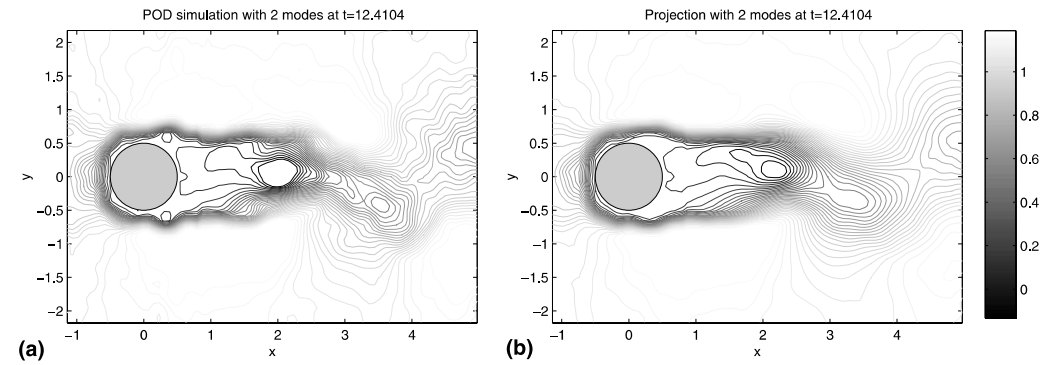

Fig. 7. Comparison of streamwise velocity contours of POD simulation and projected experimental data at $t = 12.4104$.

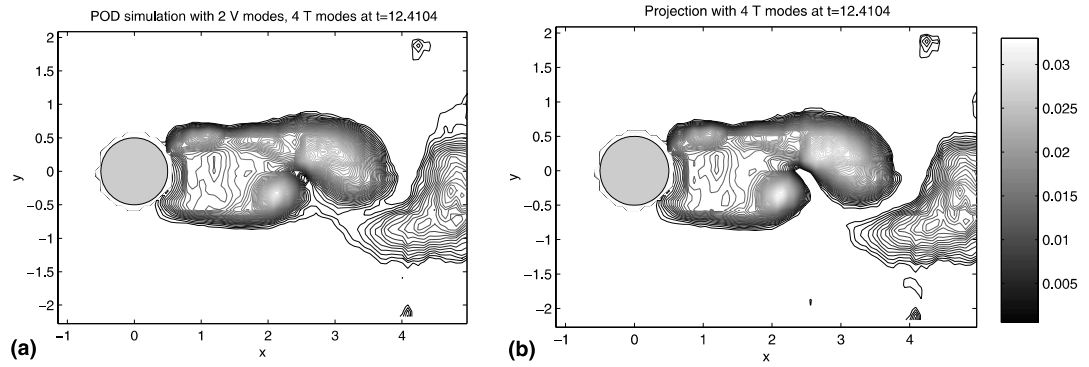

Fig. 8. Comparison of temperature contours of POD simulation and projected experimental data at $t = 12.4104$.

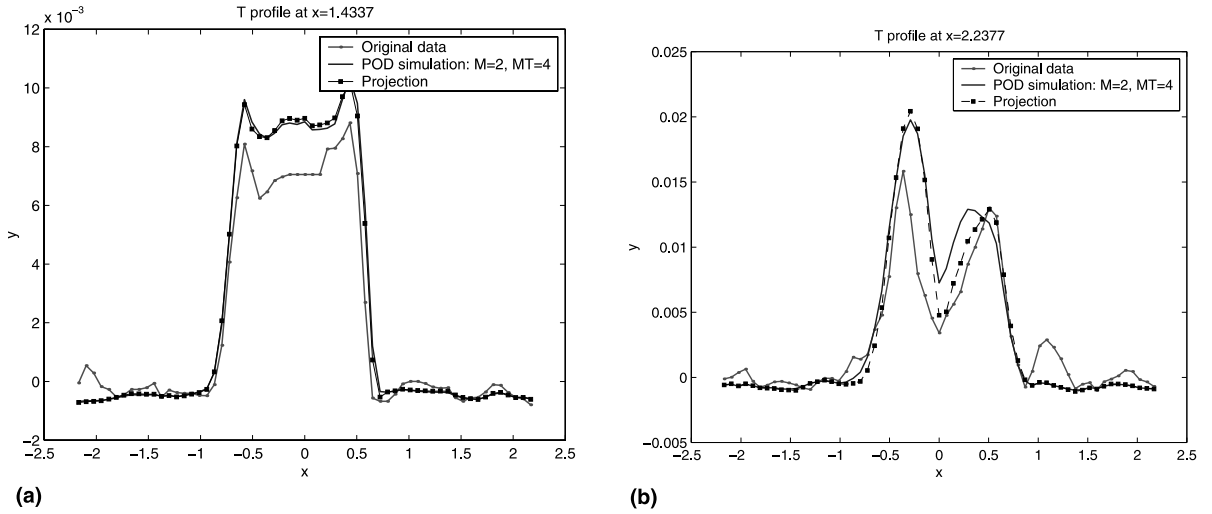

Fig. 9. Comparison of instantaneous temperature profiles of POD simulation, raw data and projected experimental data at time $t = 12.4104$ at $x/d = 1.4337$ (a) and $x/d = 2.2377$ (b).

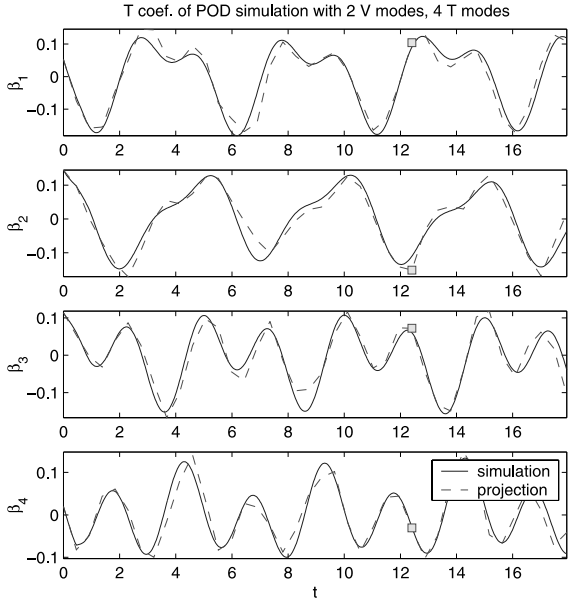

Fig. 10. Comparison of POD simulation and projection using only two velocity DPIV-based POD modes and four DPIT-based temperature modes. The time is in non-dimensional convective units.

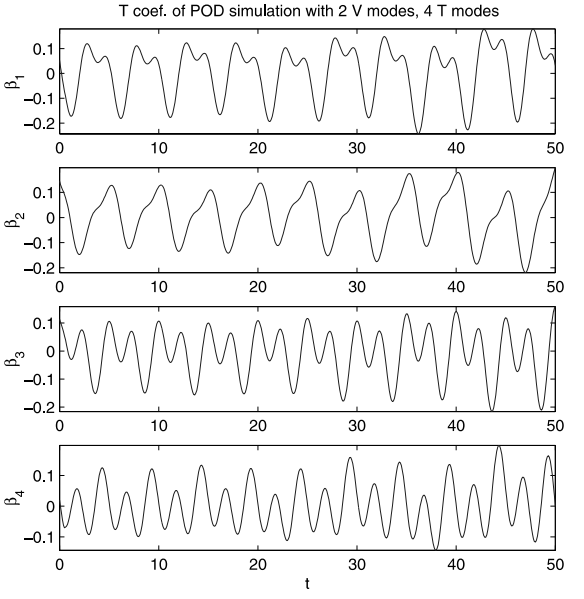

Fig. 11. Histories of temperature modal coefficients for long-time integration.

POD modes employed. This is shown in Fig. 11 that shows the time histories of the four temperature modes for about ten shedding periods. A slow increase in amplitude as time increases indicates that the coupled system diverges asymptotically.

This may not be so important from the practical point of view, especially for control-type applications where the short-term dynamics is involved. However, it is important from the theoretical point of view, and also in applications where a stationary state of the coupled system is sought. The reason that this divergence occurs, at least for the problem considered here, is attributed to inaccuracy of the high modes obtained experimentally. More specifically, the addition of high modes pollutes the dynamics of the lower more energetic modes due to

the noisy structure of such modes inherited from the experimental data.

However, the high modes can be employed to construct an approximate inertial manifold following the non-linear Galerkin method [24,25]. In particular, we consider the first few (lower) velocity modes, which primarily govern the dynamics of the flow, to be the *dominus* modes. We then think of the higher modes as *servus* modes, in a sense that they will follow the slow oscillations of the dominus (lower) modes. The higher and faster servus modes will quickly relax onto a manifold ("the steady manifold") parameterized by the dominus modes. The results of this non-linear Galerkin projection for the velocity field are shown in Fig. 12. Specifically, we compare the time histories of the velocity field corresponding to two modes only as before (straight Galerkin projection) with the corresponding results from a non-linear Galerkin projection involving the same two dominus modes and four servus modes. We see that the non-linear Galerkin projection leads to an asymptotically stable dynamical system without the need for employing explicitly ad hoc eddy viscosity models.

The direct use of experimental data in simulation is not new, however the use of simultaneous velocity and temperature *field data* and corresponding low-dimensional coupled simulations, as presented here, is new. This integration of experimental data and numerical simulation in conjunction with the dramatic reduction in the required degrees of freedom allow for *potential steering* of the experimental measurements in real time. Moreover, they provide the capability of dynamic sensitivity analysis of the most important input parameters, and predictions of new states away from the state tested in the experiments. New holographic imaging and three-dimensional DPIV/T techniques will lead to extensions of the formulation presented here to three-dimensions.

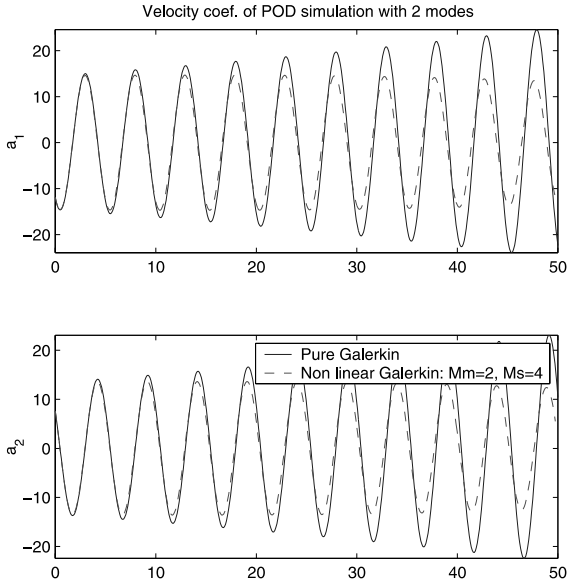

Fig. 12. Histories of velocity modal coefficients for long-time integration using Galerkin (solid-line) and non-linear Galerkin projections (dash-line).

Acknowledgements

This work was supported by a joint Brown–Caltech NSF grant. Partial support for the numerical work was also provided by DOE and ONR, and computations were performed at the Maui High Performance Supercomputing Center and at Brown's TCASV SP3.

Appendix A. Temperature Galerkin projection

We define the velocity field $\mathbf{V}(\mathbf{x},t)$ and the temperature field $\hat{T}(\mathbf{x},t)$ in a dimensionless form:

$$\mathbf{U}_f = \frac{\mathbf{V}}{\mathbf{V}_\infty}, \quad T_f = \frac{\hat{T} - T_\infty}{T_c - T_\infty}, \tag{A.1}$$

where $\mathbf{V}_\infty$ is the inlet fluid velocity, T_c is the temperature of the cylinder and T_∞ is the bulk temperature of the fluid.

Let us express the dimensionless velocity field $\mathbf{U}_f(\mathbf{x},t)$ and the dimensionless temperature field $T_f(\mathbf{x},t)$ as the sum of the mean and the time-varying part, i.e.,

$$\mathbf{U}_f(\mathbf{x},t) = \mathbf{U}(\mathbf{x}) + \mathbf{u}(\mathbf{x},t) \tag{A.2}$$

and

$$T_f(\mathbf{x},t) = T_0(\mathbf{x}) + T(\mathbf{x},t). \tag{A.3}$$

The averages in Eqs. (A.2) and (A.3) are temporal averages, i.e. the field is temporally centered. The velocity fluctuations $\mathbf{u}(\mathbf{x},t)$ can be expressed as before, as a finite expansion of bi-orthonormal functions, i.e.,

$$\mathbf{u}(\mathbf{x},t) = \sum_{m=1}^{N} \alpha_n \phi_n(\mathbf{x}), \psi_n(t), \tag{A.4}$$

where $\phi_n(\mathbf{x})$ are POD modes in the space domain and $\psi_n(t)$ are orthonormal eigenfunctions in the time domain. The temperature fluctuations $T(\mathbf{x},t)$ can be expressed as a finite expansion of bi-orthonormal functions, i.e.

$$T(\mathbf{x},t) = \sum_{m=1}^{M} \beta_m \chi_m(\mathbf{x}) \xi_m(t), \tag{A.5}$$

where $\chi_m(\mathbf{x})$ are orthonormal POD modes of temperature in the space domain and $\xi_m(t)$ are orthonormal eigenfunctions in the time domain.

The heat equation can be expressed as

$$\frac{\partial T_f}{\partial t} + \mathbf{U}_f \cdot \nabla T_f = \frac{1}{Pe}\nabla^2 T_f. \tag{A.6}$$

Let us project the heat equation onto the POD modes space

$$\left(\chi_j, \frac{\partial T_f}{\partial t} + \mathbf{U}_f \cdot \nabla T_f - \frac{1}{Pe}\nabla^2 T_f\right) = 0, \quad j = 1, \ldots, M, \tag{A.7}$$

where the operator $\cdot$ means pointwise product in the Cartesian coordinates and the operator $(,)$ means the inner product in the POD space.

Eq. (A.7) can be rewritten in the following way:

$$\left(\chi_j, \frac{\partial T_f}{\partial t}\right) + (\chi_j, \mathbf{U}_f \cdot \nabla T_f) - \left(\chi_j, \frac{1}{Pe}\nabla^2 T_f\right) = 0, \quad j = 1, \ldots, M. \tag{A.8}$$

Let us consider the first term of Eq. (A.8). By employing Eqs. (A.3) and (A.5), the first term of Eq. (A.8) becomes

$$\begin{aligned}\left(\chi_j, \frac{\partial T_f}{\partial t}\right) &= \left(\chi_j, \frac{\partial T_0(\mathbf{x})}{\partial t} + \frac{\partial T(\mathbf{x},t)}{\partial t}\right) \\ &= \left(\chi_j(\mathbf{x}), \sum_{m=1}^{M} \beta_m \chi_m(\mathbf{x}) \frac{\mathrm{d}\xi_m(t)}{\mathrm{d}t}\right), \quad j = 1, \ldots, M.\end{aligned} \tag{A.9}$$

Since the POD modes are orthonormal, Eq. (A.9) can be rewritten as

$$\left(\chi_j, \frac{\partial T_f}{\partial t}\right) = \beta_j \frac{\mathrm{d}\xi_j(t)}{\mathrm{d}t}, \quad j = 1 \ldots M. \tag{A.10}$$

Let us consider now the second term of Eq. (A.8). By employing Eqs. (A.2)–(A.5), the second term of Eq. (A.8) can be rewritten as

$$\begin{aligned}&(\chi_j, \mathbf{U}_f \cdot \nabla T_f) \\ &= (\chi_j, (\mathbf{U} + \mathbf{u}) \cdot \nabla (T_0 + T)) \\ &= (\chi_j, \mathbf{U} \cdot \nabla T_0 + \mathbf{U} \cdot \nabla T + \mathbf{u} \cdot \nabla T_0 + \mathbf{u} \cdot \nabla T) \\ &= (\chi_j(\mathbf{x}), \mathbf{U}(\mathbf{x}) \cdot \nabla T_0(\mathbf{x})) \\ &\quad + \left(\chi_j(\mathbf{x}), \mathbf{U}(\mathbf{x}) \cdot \sum_{m=1}^{M} \beta_m \nabla \chi_m(\mathbf{x}) \xi_m(t)\right) \\ &\quad + \left(\chi_j(\mathbf{x}), \sum_{n=1}^{N} \alpha_n \phi_n(\mathbf{x}) \psi_n(t) \cdot \nabla T_0(\mathbf{x})\right) \\ &\quad + \left(\chi_j(\mathbf{x}), \sum_{n=1}^{N}\sum_{m=1}^{M} \alpha_n \phi_n(\mathbf{x}) \psi_n(t) \cdot \nabla (\beta_m \chi_m(\mathbf{x}) \xi_m(t))\right), \\ &\quad j = 1, \ldots, M.\end{aligned} \tag{A.11}$$

Let us consider now the third term of Eq. (A.8). By employing Eqs. (A.3) and (A.5), the third term of Eq. (A.8) can be rewritten as

$$\begin{aligned}\left(\chi_j, \frac{1}{Pe}\nabla^2 T_f\right) &= \left(\chi_j, \frac{1}{Pe}\nabla^2 (T_0 + T)\right) \\ &= \left(\chi_j(\mathbf{x}), \frac{1}{Pe}\nabla^2 T_0(\mathbf{x})\right) \\ &\quad + \left(\chi_j(\mathbf{x}), \frac{1}{Pe}\sum_{m=1}^{M} \beta_m \nabla^2 \chi_m(\mathbf{x}) \xi_m(t)\right), \\ &\quad j = 1, \ldots, M.\end{aligned} \tag{A.12}$$

The first term on the right-hand side of Eq. (A.12) can be rewritten as

$$\left(\chi_j(\mathbf{x}), \frac{1}{Pe}\nabla^2 T_0(\mathbf{x})\right) = \frac{1}{Pe}\int_V \chi_j(\mathbf{x}) \nabla^2 T_0(\mathbf{x})\,\mathrm{d}\mathbf{x}, \quad j = 1, \ldots, M. \tag{A.13}$$

Integrating equation (A.13) by parts we obtain

$$\frac{1}{Pe}\int_V \nabla \cdot (\chi_j(\mathbf{x}) \nabla T_0(\mathbf{x}))\,\mathrm{d}\mathbf{x} - \frac{1}{Pe}\int_V \nabla \chi_j(\mathbf{x}) \cdot \nabla T_0(\mathbf{x})\,\mathrm{d}\mathbf{x}, \tag{A.14}$$

and by using the Gauss's theorem, Eq. (A.14) can be rewritten as

$$\frac{1}{Pe}\int_{\partial V} \chi_j(\mathbf{x}) \nabla T_0(\mathbf{x}) \cdot \mathbf{n}\,\mathrm{d}\mathbf{x} - \frac{1}{Pe}\int_V \nabla \chi_j(\mathbf{x}) \cdot \nabla T_0(\mathbf{x})\,\mathrm{d}\mathbf{x}. \tag{A.15}$$

Since the heat flux on the boundary is zero and the temperature of the cylinder surface is zero, the first term of (A.15) is zero and (A.13) becomes

$$\left(\chi_j(\mathbf{x}), \frac{1}{Pe}\nabla^2 T_0(\mathbf{x})\right) = -\frac{1}{Pe}\int_V \nabla \chi_j(\mathbf{x}) \cdot \nabla T_0(\mathbf{x})\,\mathrm{d}\mathbf{x}. \tag{A.16}$$

The second term on the right-hand side of Eq. (A.12) can be rewritten as

$$\begin{aligned}&\left(\chi_j(\mathbf{x}), \frac{1}{Pe}\sum_{m=1}^{M} \beta_m \nabla^2 \chi_m(\mathbf{x}) \xi_m(t)\right) \\ &\quad = \frac{1}{Pe}\sum_{m=1}^{M} \beta_m \xi_m(t) \int_V \chi_j(\mathbf{x}) \nabla^2 \chi_m(\mathbf{x})\,\mathrm{d}\mathbf{x}, \\ &\quad j = 1, \ldots, M.\end{aligned} \tag{A.17}$$

Integrating by parts equation (A.17) we obtain

$$\frac{1}{Pe}\sum_{m=1}^{M} \beta_m \xi_m(t)\left(\int_V \nabla \cdot (\chi_j(\mathbf{x}) \nabla \chi_m(\mathbf{x}))\,\mathrm{d}\mathbf{x} - \int_V \nabla \chi_j(\mathbf{x}) \cdot \nabla \chi_m(\mathbf{x})\,\mathrm{d}\mathbf{x}\right), \tag{A.18}$$

and by using the Gauss theorem, Eq. (A.18) can be re-written as

$$\frac{1}{Pe}\sum_{m=1}^{M}\beta_m\xi_m(t)\left(\int_{\partial V}\chi_j(\mathbf{x})\nabla\chi_m(\mathbf{x})\cdot\mathbf{n}\,\mathrm{d}\mathbf{x} - \int_V \nabla\chi_j(\mathbf{x})\cdot\nabla\chi_m(\mathbf{x})\right)\mathrm{d}\mathbf{x}. \tag{A.19}$$

Since the heat flux on the boundary is zero and the temperature of the cylinder surface is zero, the first term of (A.19) is zero and (A.17) becomes

$$\left(\chi_j(\mathbf{x}),\frac{1}{Pe}\sum_{m=1}^{M}\beta_m\nabla^2\chi_m(\mathbf{x})\xi_m(t)\right) = -\frac{1}{Pe}\sum_{m=1}^{M}\beta_m\xi_m(t)\int_V\nabla\chi_j(\mathbf{x})\cdot\nabla\chi_m(\mathbf{x}))\,\mathrm{d}\mathbf{x}, \quad j=1,\ldots,M. \tag{A.20}$$

Now, substituting Eqs. (A.10), (A.11), (A.16) and (A.20) in Eq. (A.8) we obtain the following for the unknowns $\xi_j(t)$:

$$\begin{aligned}\beta_j\frac{\mathrm{d}\xi_j(t)}{\mathrm{d}t} &+ (\chi_j(\mathbf{x}),\mathbf{U}(\mathbf{x})\cdot\nabla T_0(\mathbf{x})) \\ &+\left(\chi_j(\mathbf{x}),\mathbf{U}(\mathbf{x})\cdot\sum_{m=1}^{M}\beta_m\nabla\chi_m(\mathbf{x})\xi_m(t)\right) \\ &+\left(\chi_j(\mathbf{x}),\sum_{n=1}^{N}\alpha_n\phi_n(\mathbf{x})\psi_n(t)\cdot\nabla T_0(\mathbf{x})\right) \\ &+\left(\chi_j(\mathbf{x}),\sum_{m=1}^{M}\sum_{n=1}^{N}\alpha_n\phi_n(\mathbf{x})\psi_n(t)\cdot\nabla(\beta_m\chi_m(\mathbf{x})\xi_m(t))\right) \\ &+\frac{1}{Pe}(\chi_j(\mathbf{x}),\nabla T_0(\mathbf{x})) \\ &+\frac{1}{Pe}\sum_{m=1}^{M}\beta_m\xi_m(t)(\nabla\chi_j(\mathbf{x}),\nabla\chi_m(\mathbf{x}))=0, \\ j&=1,\ldots,M.\end{aligned} \tag{A.21}$$

We solved Eq. (A.21) with a fourth-order Runge–Kutta method.

References

[1] J.C. Robinson, A rigorous treatment of 'experimental' observations for the two-dimensional Navier–Stokes equations, Proc. R. Soc. London A 457 (2001) 1007.

[2] X. Ma, G.-S. Karamanos, G.E. Karniadakis, Dynamics and low-dimensionality in the turbulent near-wake, J. Fluid Mech. 401 (2000) 29.

[3] A. Liakopoulos, P.A. Blythe, H. Gunes, A reduced dynamical model of convective flows in tall laterally heated cavities, Proc. R. Soc. London A 453 (1997) 663.

[4] H.M. Park, W.S. Jung, The Karhunen–Loeve Galerkin method for the inverse natural convection problems, Int. J. Heat Mass Transfer 44 (2001) 155–167.

[5] A.E. Deane, I.G. Kevrekidis, G.E. Karniadakis, S.A. Orszag, Low-dimensional models for complex geometry flows: application to grooved channels and circular cylinders, Phys. Fluids 3 (10) (1991) 2337.

[6] N.-Z. Cao, N. Aubry, Detection of self-similar structures in turbulence: application to wake flows, in: Proceedings of IUTAM Symposium: Eddy Structure Identification in Free Turbulent Shear Flows, Poitiers, France, 1992.

[7] X. Ma, Hierarchical Galerkin and non-linear Galerkin models for laminar and turbulent wakes, Ph.D. Thesis, Brown University, 2001.

[8] P.F. Batcho, G.E. Karniadakis, Generalized Stokes eigenfunctions: a new trial basis for the solution of incompressible Navier–Stokes equations, J. Comput. Phys. 115 (1994) 121.

[9] A.K. Bangia, P.F. Batcho, I.G. Kevrekidis, G.E. Karniadakis, Unsteady 2-d flows in complex geometries: comparative bifurcation studies with global eigenfunction expansions, SIAM J. Sci. Comput. 18 (1997) 775–805.

[10] G. Berkooz, P. Holmes, J.L. Lumley, The proper orthogonal decomposition in the analysis of turbulent flows, Annu. Rev. Fluid Mech. 25 (1993) 537.

[11] K.S. Ball, L. Sirovich, L.R. Keefe, Dynamical eigenfunction decomposition of turbulent channel flow, Int. J. Numer. Meth. Fluids 12 (1991) 585.

[12] M.N. Glauser, W.K. George, Orthogonal decomposition of the axisymmetric jet mixing layer including azimuthal dependence, in: G. Comte-Bellot, J. Mathieu (Eds.), Advances in Turbulence, Springer, New York, 1987.

[13] A. Glezer, Z. Kadioglu, A.J. Pearlstein, Development of an extended proper orthogonal decomposition and its application to a time periodically forced plane mixing layer, Phys. Fluids 1 (8) (1989) 1363.

[14] A. Vernet, G.A. Kopp, J.A. Ferre, F. Giralt, Simultaneous velocity and temperature patterns in the far region of a turbulent cylinder wake, J. Fluid Eng. 119 (1997) 463.

[15] N. Aubry, P. Holmes, J.L. Stone, J.L. Lumley, The dynamics of coherent structures in the wall region of a turbulent boundary layer, J. Fluid Mech. 192 (1988) 115.

[16] D. Rempfer, H.F. Fasel, Evolution of three-dimensional coherent structures in a flat-plate boundary layer, J. Fluid Mech. 260 (1994) 351.

[17] C.E. Willert, M. Gharib, Digital particle-image velocimetry, Exp. Fluids 10 (1991) 181.

[18] D. Dabiri, M. Gharib, Digital particle image thermometry: the method and implementation, Exp. Fluids 11 (1991) 77.

[19] H.G. Park, D. Dabiri, M. Gharib, Digital particle image velocimetry/thermometry and application to wake of a heated circular cylinder, Exp. Fluids 30 (2001) 327.

[20] G.E. Karniadakis, S.J. Sherwin, Spectral/hp Element Methods for CFD, Oxford University Press, Oxford, 1999.

[21] H.G. Park, A study of heat transport processes in the wake of a stationary and oscillating circular cylinder using digital particle image velocimetry/thermometry. Ph.D. Thesis, California Institute of Technology, 1998.

[22] F. Noca, H. Park, M. Gharib, Vortex formation length of a circular cylinder ($300 < Re < 4000$) using DPIV, in: Proceedings on Bluff Body Wakes and Vortex-Induced Vibration, ASME Fluids Engineering Division, Washington, DC, 21–25 June, 1998.

[23] C. Norberg, An experimental investigation of the flow around a circular cylinder: influence of aspect ratio, J. Fluid Mech. 258 (1994) 287.
[24] C. Foias, O. Manley, R. Temam, Modelling of the interaction of small and large eddies in two-dimensional turbulent flows, Math. Modelling Numer. Anal. 22 (1988) 93–118.
[25] R. Temam, Approximation of attractors, large scale simulations and multiscale methods, Proc. R. Soc. London A 434 (1991) 23–39.